

Urban Traffic Accident Risk Prediction Revisited: Regionality, Proximity, Similarity and Sparsity

Minxiao Chen
Beijing University of Posts and
Telecommunications
Beijing, China
Beiyou Shenzhen Institute
Beijing, China
chenminxiao@bupt.edu.cn

Haitao Yuan*
Nanyang Technological University
Singapore
haitao.yuan@ntu.edu.sg

Nan Jiang
Beijing University of Posts and
Telecommunications
Beijing, China
Beiyou Shenzhen Institute
Beijing, China
jn_bupt@bupt.edu.cn

Zhifeng Bao
The Royal Melbourne Institute of
Technology
Melbourne, Australia
zhifeng.bao@rmit.edu.au

Shangguang Wang
Beiyou Shenzhen Institute
Beijing, China
Beijing University of Posts and
Telecommunications
Beijing, China
sgwang@bupt.edu.cn

Abstract

Traffic accidents pose a significant risk to human health and property safety. Therefore, to prevent traffic accidents, predicting their risks has garnered growing interest. We argue that a desired prediction solution should demonstrate resilience to the complexity of traffic accidents. In particular, it should adequately consider the regional background, accurately capture both spatial proximity and semantic similarity, and effectively address the sparsity of traffic accidents. However, these factors are often overlooked or difficult to incorporate. In this paper, we propose a novel multi-granularity hierarchical spatio-temporal network. Initially, we innovate by incorporating remote sensing data, facilitating the creation of hierarchical multi-granularity structure and the comprehension of regional background. We construct multiple high-level risk prediction tasks to enhance model's ability to cope with sparsity. Subsequently, to capture both spatial proximity and semantic similarity, region feature and multi-view graph undergo encoding processes to distill effective representations. Additionally, we propose message passing and adaptive temporal attention module that bridges different granularities and dynamically captures time correlations inherent in traffic accident patterns. At last, a multivariate hierarchical loss function is devised considering the complexity of the prediction purpose. Extensive experiments on two real datasets verify the superiority of our model against the state-of-the-art methods.

*Corresponding author.

Permission to make digital or hard copies of all or part of this work for personal or classroom use is granted without fee provided that copies are not made or distributed for profit or commercial advantage and that copies bear this notice and the full citation on the first page. Copyrights for components of this work owned by others than the author(s) must be honored. Abstracting with credit is permitted. To copy otherwise, or republish, to post on servers or to redistribute to lists, requires prior specific permission and/or a fee. Request permissions from permissions@acm.org.

CIKM '24, October 21–25, 2024, Boise, ID, USA

© 2024 Copyright held by the owner/author(s). Publication rights licensed to ACM.
ACM ISBN 979-8-4007-0436-9/24/10
<https://doi.org/10.1145/3627673.3679567>

CCS Concepts

• Information systems → Spatial-temporal systems.

Keywords

Traffic accident prediction, Spatio-temporal data, Remote sensing

ACM Reference Format:

Minxiao Chen, Haitao Yuan, Nan Jiang, Zhifeng Bao, and Shangguang Wang. 2024. Urban Traffic Accident Risk Prediction Revisited: Regionality, Proximity, Similarity and Sparsity. In *Proceedings of the 33rd ACM International Conference on Information and Knowledge Management (CIKM '24)*, October 21–25, 2024, Boise, ID, USA. ACM, New York, NY, USA, 10 pages. <https://doi.org/10.1145/3627673.3679567>

1 INTRODUCTION

According to the World Health Organization (WHO) [33], approximately 1.3 million people die each year due to traffic accidents, making it a leading cause of death among children and young adults aged 5 to 29. In response, the United Nations General Assembly has set an ambitious target of halving the global number of deaths and injuries from road traffic crashes by 2030 [29]. Therefore, it is of vital importance to predict traffic accident risk accurately, which can assist government in managing traffic risks and help drivers avoid high-risk areas. When revisiting this problem, we find some critical yet missing aspects that contribute to its accuracy boost.

(1) **Regionality: Regional Background Effects.** Traffic accidents are affected by many complex factors, and the ways to which these factors affect are difficult to analyze. To capture the underlying mechanisms of traffic accidents, regional background is essential. For instance, as shown in Fig. 1, different regions may have share similar road structure (e.g., crossroads) and weather (e.g., sunny), but entirely different regional background (e.g., parking lot, lake, small park vs. dense residential area). This leads to significant variations in traffic accident patterns. However, these regional backgrounds are often overlooked and difficult to capture.

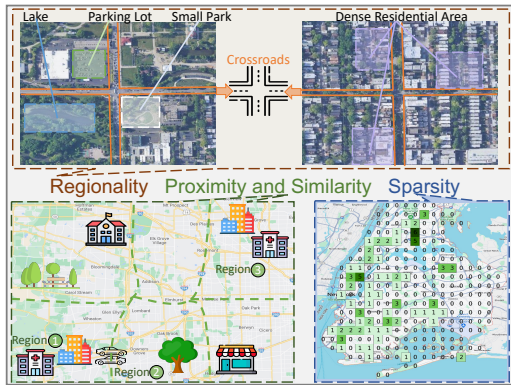


Figure 1: Critical Aspects of Traffic Accident.

(2) **Proximity and Similarity: Spatial and Semantic Correlations.** Traffic accidents exhibit dual correlation involving both spatial proximity and semantic similarity. This implies that traffic accidents occurring in close areas or areas sharing similar semantic properties tend to have high similarities [39]. For example, in Fig. 1, the adjacency of Region 1 and Region 2 suggests interconnected roads, while the similar distribution of POIs in Region 1 and Region 3 contributes to similar accident patterns. Effectively capturing both types of correlations poses a significant challenge.

(3) **Sparsity: Zero-Inflation Problem.** As shown in the lower right part of Fig. 1, the number of traffic accidents in NYC during an afternoon is presented in a heatmap. Notably, most regions experience zero traffic accidents. This is identified as the zero-inflation problem. Failure to properly address this sparsity can lead the model to generate predictions with an excessive number of zeros, rendering the predictions meaningless [21].

Unfortunately, existing studies have not thoroughly captured most of the above aspects. Traditionally, statistics-based methods [3, 6, 22, 27] merely utilize the statistics information of historical accidents, ignoring the influence of many spatio-temporal factors, which leads to poor performance. To alleviate this, learning-based methods [1, 4, 5, 26, 28, 31, 32, 38] have been proposed. They analyze spatio-temporal features to capture the correlations between traffic accidents. However, they fail to effectively capture the spatial proximity and semantic similarity of traffic accidents and miss out on the regional background of where they occur. Worse still, their approach to dealing with sparsity is not sufficiently effective.

To incorporate all the above critical aspects, we design a Multi-Granularity Hierarchical Spatio-Temporal Network (MGHSTN) for traffic accident risk prediction.

First, recognizing the **informative potential of remote sensing images in revealing regional backgrounds**, we integrate them into the traffic accident risk prediction process. This innovative addition serves a dual purpose: enhancing the spatio-temporal feature set and aiding in semantic analysis. We achieve this by converting remote sensing images into spatial features, augmenting the data. Simultaneously, we introduce a self-supervised autoencoder to encode these images for enhanced semantic understanding.

Second, to capture geographical correlations, following the first law of geography in geography science, we **utilize spatio-temporal region features that encompass the geographical layout of the regions** to capture the physical proximity between different

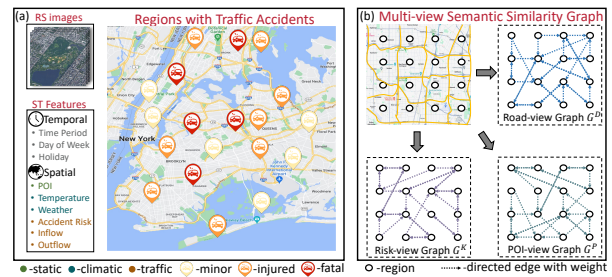


Figure 2: An illustration of preliminaries, (a) shows the region features input and (b) shows the graph features input.

areas. Additionally, to capture traffic correlations, we **construct a multi-view semantic similarity graph that quantifies the semantic similarities among regions** based on attributes like Points of Interest (POI) distributions. By integrating these two components, we lay the foundation for a model that inherently considers both spatial and semantic aspects.

Third, to address the zero-inflation problem, motivated by the idea of aggregation, we **enhance the risk prediction at the lowest level by introducing multiple high-level risk prediction tasks**, carefully tailored to low-sparsity data settings. In particular, we use regularized region partition and graph clustering to respectively construct hierarchical structures based on spatio-temporal region features and semantic graph features. In addition, we design a multi-level embedding fusion mechanism to fully leverage the hierarchical structure for mutual learning of different levels. Furthermore, we devise an adaptive temporal attention module to acquire temporal dependencies from the representations encoded by preceding modules, effectively harnessing the attention mechanism to adeptly capture correlations. Finally, we design a multivariate loss function to learn the proposed model comprehensively.

In summary, we make the following contributions:

- We design a multi-granularity hierarchical spatio-temporal network, MGHSTN, that can fully exploit spatio-temporal features in traffic accidents in hierarchical manner. (Sec. 3)
- We incorporate remote sensing images to enhance regional background comprehension and create multi-level hierarchical structures for both region feature and multi-view graph. (Sec. 3.1)
- We design multiple encoding modules for multi-source spatio-temporal features and propose a cross-level message passing module to enable mutual learning across different levels. (Sec. 3.2)
- We comprehensively model the traffic accident risk prediction problem by designing a multivariate loss function to cater to the multi-faceted objective of prediction. (Sec. 3.3)
- We conduct a comprehensive evaluation on two real-world datasets. The results show that our method significantly outperforms state-of-the-art in terms of accuracy and robustness. (Sec. 4)

2 PROBLEM FORMULATION

In this section, we first introduce some useful preliminaries. Then we formalize the traffic accident risk prediction problem.

2.1 Preliminaries

Region. In accordance with established urban zoning, the city is divided into N regions based on administrative divisions. Each of

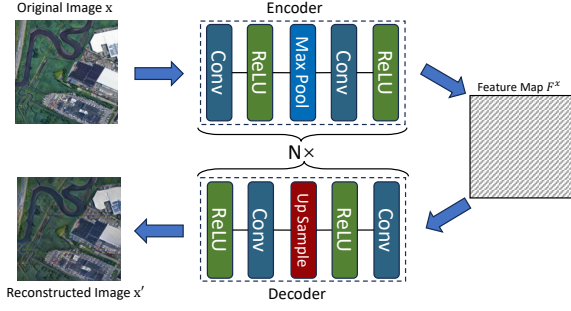


Figure 4: The Framework of Remote Sensing Autoencoder

we aggregate the finest granularity data to obtain coarser-grained hierarchical data. Considering ST contains multi-source features, which have different statistical characteristics, therefore we utilize the *maximum*, *mean* and *summation* methods respectively for aggregation. For instance, the maximum method can ensure that no weather conditions are lost after aggregation, the average method can determine the appropriate temperature of aggregated grids, and the summation method can reasonably obtain the aggregated value for traffic accident risk.

3.1.3 Multi-view Graph Construction. Traffic accidents show a connection that can be largely understood by analyzing semantic features on the ground, such as POIs and road structures [18]. Based on the semantic features, we construct three semantic similarity graphs, namely the road-view similarity graph $G^D = (V, E^D)$, the risk-view similarity graph $G^K = (V, E^K)$ and the POI-view similarity graph $G^P = (V, E^P)$.

To represent the similarity of road, risk, and POI between any two nodes, we use Jensen-Shannon divergence [19] to calculate the similarity score. Taking the POI similarity as an example, it can be computed by the following equation:

$$Sim_P(U_i, U_j) = 1 - JS(R_p^i, R_p^j) \quad (2)$$

$$JS(R_p^i, R_p^j) = \frac{1}{2} \sum_{d=1}^D \left(\log \frac{2R_p^i(d)R_p^j(d) + 2R_p^j(d)R_p^i(d)}{R_p^i(d) + R_p^j(d)} \right) \quad (3)$$

where R_p^i, R_p^j denote the POI distribution of region U_i and U_j and D is the dimension of POI information. Similarly, we also calculate $Sim_D(U_i, U_j)$ and $Sim_K(U_i, U_j)$ for road-view and risk-view.

Afterwards, we use the semantic similarity calculated between each pair of nodes as the weight and select the Top- K most similar nodes as neighbors for each node. Finally, we construct adjacency matrices $M_A = [M_A^D, M_A^K, M_A^P] \in \mathbb{R}^{N \times N}$ for three different views, where N is the number of regions.

The adjacency matrices represent global semantic similarity structures between regions, but has no specific node features. Therefore, we use traffic features (i.e., traffic accident risk map, inflow, outflow) as node features $M_n^t \in \mathbb{R}^{N \times d_c}$ for each time interval t . Finally, we perform matrix multiplication between the adjacency matrices M_A of the three views and the node features M_n^t separately to get multi-view semantic similarity graph $G^t = M_A \cdot M_n^t$.

3.1.4 Pre-train & Remote Sensing Embedding. Remote sensing images can provide regional information, which can be encoded as remote sensing features F_{rs} as done in Sec. 3.1.1. For multi-level

graph construction, we further mine them from another perspective, the perspective of similarity clustering. Aiming to learn the semantic properties of remote sensing images, autoencoder can be trained as a feature extractor by minimizing the reconstruction error between input and output data [17]. To obtain remote sensing embeddings as much as possible from the global perspective, as shown in Fig. 4, we propose a remote sensing autoencoder. The entire process of remote sensing autoencoder is as follows:

$$\begin{aligned} F_k^x &= \sigma(\text{MaxPool}(\sigma(W_k^{(E_0)} * F_{k-1}^x + b_k^{(E_0)})) * W_k^{(E_1)} + b_k^{(E_1)}) \\ x'_k &= \sigma(\text{UpSample}(\sigma(W_k^{(D_0)} * x'_{k-1} + b_k^{(D_0)})) * W_k^{(D_1)} + b_k^{(D_1)}) \end{aligned} \quad (4)$$

where $*$ represents convolution operation, F_k^x is the feature map of k -th encoder, $\sigma(\cdot)$ is the ReLU activation function, W_k, b_k are trainable weights, x'_k is the reconstructed image of k -th decoder.

In this work, we pre-train the autoencoder from scratch by using two different losses, which can be computed as follows:

$$\begin{aligned} loss_{pp}(x, x') &= \frac{1}{c' \cdot h' \cdot w'} \cdot \sum_{i=1}^{c'} \sum_{j=1}^{h'} \sum_{k=1}^{w'} (x_{ijk} - x'_{ijk})^2 \\ loss_{feat}(F_{ij}^x, F_{ij}^{x'}) &= \frac{1}{c' \cdot h' \cdot w'} \cdot \sum_{i=1}^c \sum_{j=1}^{h \cdot w} (F_{ij}^x - F_{ij}^{x'})^2 \end{aligned} \quad (5)$$

where $loss_{pp}$ is the per-pixel loss, forces the pixel value of x' to resemble the ones of x . F^x and $F^{x'}$ are the feature maps obtained by encoding input image x and reconstructed output image x' . $loss_{feat}$ is the feature loss, measures the difference between the feature maps F^x and the feature maps $F^{x'}$. After pre-training, we separately use the encoder part to obtain remote sensing embeddings E^{rs}

3.1.5 Multi-level Graph Construction. To construct hierarchical graph structure, we propose Algorithm 1 for hierarchical graph clustering to get hierarchical aggregation relationships \mathcal{R}_a .

Algorithm 1: Hierarchical Graph Clustering

Input: RS embedding E^{rs} , part number $[N_1, N_2, \dots, N_n]$, graph size $[\mathcal{L}_1, \mathcal{L}_2, \dots, \mathcal{L}_n]$, granularity number n
Output: hierarchical aggregation relationships \mathcal{R}_a

- 1 build RS similarity graph $G_{g^1}^{rs}$ at granularity g^1 with E^{rs} ;
- 2 **for** $i \leftarrow 1 \dots n$ **do**
- 3 $M_i \leftarrow \text{graphPartition}(N_i, \mathcal{L}_i, G_{g^i}^{rs})$;
- 4 $\mathcal{P}_i \leftarrow \text{extract}(M_i)$;
- 5 $X_{i+1}^{rs} \leftarrow \text{averageAggregate}(\mathcal{P}_i, X_i^{rs})$;
- 6 build next level RS similarity graph $G_{g^{i+1}}^{rs}$ with X_{i+1}^{rs} ;
- 7 $\mathcal{R}_a \leftarrow [\mathcal{P}_1, \dots, \mathcal{P}_n]$;
- 8 **return** \mathcal{R}_a

Firstly, we construct a novel remote sensing similarity graph denoted as $G^{rs} = (V, E^{rs})$. We represent regions as nodes and use the remote sensing embedding E^{rs} as node features. We then establish edges E^{rs} between adjacent nodes based on spatial relationships. The weight of each edge between adjacent nodes is determined by the cosine similarity $\cos(E_i^{rs}, E_j^{rs})$.

Next, to classify nodes with similar remote sensing features and close spatial distances into the same category, we choose the classic graph clustering algorithm Metis [15]. Its primary goal is to

create partitions that are roughly equal in size while minimizing the number of "edges cut" (i.e., edges that cross between different parts). For the remote sensing similarity graph $G_{g^i}^{rs}$, we employ graph partition to obtain membership sets \mathcal{M}_i for all subgraphs. We then extract node parts \mathcal{P}_i from \mathcal{M}_i and calculate the next level remote sensing embedding $E_{g^{i+1}}^{rs}$ based on \mathcal{P}_i and E_i^{rs} .

Then, we construct $G_{g^{i+1}}^{rs}$ based on $E_{g^{i+1}}^{rs}$, and repeat the above procedures until $i = n$, where n is number of granularity levels. We use the pre-computed part number list $[\mathcal{N}_1, \mathcal{N}_2, \dots, \mathcal{N}_n]$ and graph size list $[\mathcal{L}_1, \mathcal{L}_2, \dots, \mathcal{L}_n]$ for each level's graph partition.

Finally, we get the hierarchical aggregation relationships \mathcal{R}_a by combining node parts $[\mathcal{P}_1, \dots, \mathcal{P}_n]$ from each level.

To construct the hierarchical graph structure, we take the original multi-view graph G as the finest-grained basis and perform hierarchical aggregation on it according to \mathcal{R}_a . Specifically, we construct data for each granularity in a hierarchical manner from fine to coarse, which can be outlined as the following process:

- ① Firstly, based on the hierarchical aggregation relationship \mathcal{R}_a , we aggregate the node set V_{g^i} of the last granularity g^i to obtain a new node set $V_{g^{i+1}}$ for the current granularity g^{i+1} .
- ② Then, the current granularity's graph inherit the connectivity of the last granularity's graph (e.g., for the current granularity's nodes $V_{g^{i+1}}^A$ and $V_{g^{i+1}}^B$ aggregated from last granularity's nodes $[V_{g^i}^a, \dots]$ and $[V_{g^i}^b, \dots]$, there is an edge between $V_{g^i}^a$ and $V_{g^i}^b$ as long as there is an edge between any $V_{g^i}^a \in V_{g^i}^A$ and any $V_{g^i}^b \in V_{g^i}^B$).
- ③ Next, for edges at the current granularity, we use the maximum edge weight associated with it from the last level as its weight.
- ④ Finally, to maintain consistency with the initial graph, we only keep the top K edges with highest weights for each node.

This process leads to the creation of semantically rich and hierarchically structured graphs.

3.2 Feature Encoding

In this section, we address the distinctive characteristics of geography, traffic and time series by introducing dedicated modules for their encoding: the *Region Feature Encoding* in Sec. 3.2.1 to capture spatial proximity, the *Graph Feature Encoding* in Sec. 3.2.2 to capture semantic similarity and the *Time Series Correlation Capture* in Sec. 3.2.3 to capture time series dependencies.

3.2.1 Region Feature Encoding. According to previous studies [26, 31, 32, 41], for a specific region, the traffic accident risk of its target time interval is highly correlated with several previous time intervals on the same day and the same time interval several weeks prior, which is known as the short-term proximity and long-term periodicity. To this end, for all granularity g^* , we fetch region features from the previous p time intervals and the same time interval in previous q weeks as the historical observation sequence, whose length is $T = p + q$. Considering the relationships between region features and traffic accidents are highly dependent on the geographical spatial correlation between grids, we utilize convolutions to capture this correlation, which can be formulated as:

$$H_g^{t,k} = \sigma(W_g^k * H_g^{t,k-1} + b_g^k) \quad (6)$$

where $*$ represents convolution operation, $\sigma(\cdot)$ is the ReLU activation function, W_g^k, b_g^k are trainable weights, $H_g^{t,k}$ is the output of the k -th convolutional layer at time interval t for granularity g .

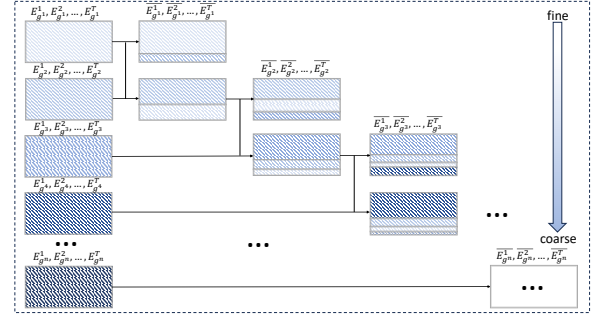


Figure 5: Multi-level Embedding Fusion Mechanism

3.2.2 Graph Feature Encoding. Firstly, similar to region feature, we construct a graph historical observation sequence consisting of short-term and long-term for each granularity. Afterwards, aiming to model the semantic correlation between regions, we leverage graph convolution to learn node representations for the semantic similarity graph $G_{g^*} = [G_{g^*}^D, G_{g^*}^K, G_{g^*}^P]$ at each granularity g , which is computed as follows:

$$E_g^t = \sigma(\sigma(G_g^t W_g^{(0)} + b_g^{(0)}) W_g^{(1)} + b_g^{(1)}) \quad (7)$$

where W_g, b_g are trainable weights, $\sigma(\cdot)$ is the ReLU activation function, E_g^t is the embedding of semantic similarity graph.

In Sec. 3.1.5, we perform hierarchical graph clustering based on remote sensing similarity, aiming to construct multi-level graph, which results in coarse-grained graph nodes having more accident counts. To enhance prediction at the finest-grained level and capture spatial relationships across varying granularities, we propose multi-level embedding fusion module. As shown in Fig. 5, the information transfer between different granularity levels is based on the hierarchical aggregation relationship \mathcal{R}_a . Since each coarse-grained graph node is composed of several fine-grained graph nodes, there is an aggregation relationship between adjacent levels. Based on that, we propose the following procedure:

1. Firstly, we construct a granularity transformation matrix M_{tran} for any two adjacent layers based on \mathcal{R}_a as follows:

$$M_{tran}(i, j) = \begin{cases} 1 & \text{if } U_{g^{fine}}^i \in U_{g^{coarse}}^j \\ 0 & \text{otherwise} \end{cases} \quad (8)$$

where $U_{g^{fine}}^i$ denotes the region i of granularity g^{fine} and $U_{g^{coarse}}^j$ denotes the region j of granularity g^{coarse} .

2. Then, for any two adjacent layers, we use the following equation to perform embedding fusion:

$$\begin{aligned} \overline{E}_{g^{coarse}} &= E_{g^{coarse}} + \lambda_f M_{tran}^T E_{g^{fine}} \\ \overline{E}_{g^{fine}} &= E_{g^{fine}} + \lambda_c M_{tran} E_{g^{coarse}} \end{aligned} \quad (9)$$

where λ_f and λ_c are the fusion coefficient of relatively fine layer and coarse layer.

3. Finally, we repeat step 2 from fine to coarse, generating fused embedding \overline{E}_g for each granularity level. The output sequence of this module is denoted as $\{\overline{E}\} = \{\overline{E}^1, \overline{E}^2, \dots, \overline{E}^T\}$

3.2.3 Time Series Correlation Capture. So far, the model has completed preliminary feature encoding. To fully capture the short-term proximity and long-term periodicity, as shown in Fig. 6, we propose

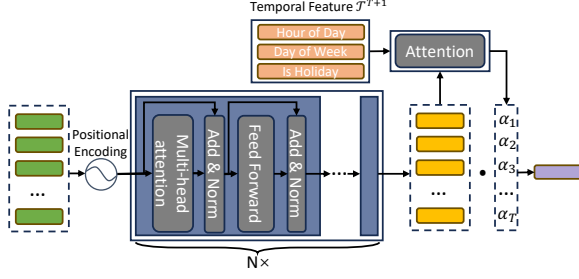


Figure 6: Illustration of Adaptive Temporal Attention Module

an adaptive temporal attention module. Specifically, taking the output sequence $\{H\}$ of the *region feature encoding* as an example, we first follow the mechanism proposed in [30] to perform positional encoding. For each element H^t in the sequence, it corresponds to a positional encoding $H_o^t \in \mathbb{R}^{d_{st}}$, which is computed as follows:

$$\begin{aligned} H_o^t[2k] &= \sin(t/10000^{\frac{2k}{d_{st}}}) \\ H_o^t[2k+1] &= \cos(t/10000^{\frac{2k}{d_{st}}}) \end{aligned} \quad (10)$$

where $H_o^t[2k]$ and $H_o^t[2k+1]$ correspond to even and odd dimensions of H_o^t , respectively. Next, we apply N self-attention blocks to convert the code H^t into the code \bar{H}^t for each time interval t . Specifically, each block includes the following steps:

1. **Self-attention:** For each code H^t , we first generate *query* ($Q^t = W_q H^t$), *key* ($K^t = W_k H^t$) and *value* ($V^t = W_v H^t$). Then, we compute the $score(t, t') = \text{softmax}(\frac{Q^t K^{t'}}{\sqrt{d_{st}}})$. Afterwards, the code H^t would be converted into a new representation (i.e., $z_a^t = \sum_{t'} score(t, t') V^{t'}$).
2. **Add & Normalize:** We leverage ResNet [10] and the layer-normalization [2] to accelerate the training process. Hence, the code would be updated: $\bar{H}^t = LN(\bar{H}^t \oplus z_a^t)$
3. **Feed Forward:** For each updated code, we further encode it with a fully connected layer: $z_f^t = ReLU(W_f \bar{H}^t + b_f)$.
4. **Add & Normalize:** Similar to step 2, the code is updated as following: $\bar{H}^t = LN(\bar{H}^t \oplus z_f^t)$

For simplicity, we denote the above four steps in the i -th block for granularity g as $SAB_g^i(\cdot)$. Thus, the sequence $\{\bar{H}_g\}$ is generated by N self-attention blocks, which can be formulated as below:

$$\{\bar{H}_g\} = SAB_N(SAB_{N-1}(\dots SAB_1(\{H_g\}))) \quad (11)$$

Considering that the sequence $\{H\}$ is composed of historical observations from different time intervals, each element H^t in sequence has different impact on the traffic accident situation at target time interval $T+1$, we introduce a temporal attention mechanism to adaptively capture the dynamic correlation between historical observations and target interval. Specifically, we first calculate the attention scores between $\{\bar{H}\}$ and target time interval's temporal feature \mathcal{T}^{T+1} , and use them as weights for summation to obtain the final output $\{\hat{H}\}$, which can be formulated as follows:

$$\alpha = \text{softmax}(ReLU(\{\bar{H}\}W_H + \mathcal{T}^{T+1}W_T + b_\alpha)) \quad (12)$$

$$\{\hat{H}\} = \sum_{i=1}^T \alpha_i \cdot \bar{h}^i \quad (13)$$

where W_H , W_T and b_α are trainable weights, $\alpha \in \mathbb{R}^T$ is the attention score vector, which can be considered as the importance distribution of different historical observation. Similarly, for the output sequence $\{E\}$ of the cross-granularity message passing part, the same adaptive temporal attention module is adopted to obtain $\{\hat{E}\}$.

3.3 Fusion Prediction

First, we fuse each pair of $\{\hat{H}_g\}$ and $\{\hat{E}_g\}$, which are the final encoding of region features and graph features. Considering that they are obtained from different form of data, thus have different degrees of influence on the target region, we therefore adapt two trainable weight matrices and a fully connected layer to dynamically fuse them, which can be formulated as below:

$$\hat{A}_g^{T+1} = FC(W_1\{\hat{H}_g\} + W_2\{\hat{E}_g\}) \quad (14)$$

where W_1 and W_2 are trainable weights, and \hat{A}_g^{T+1} is the traffic accident risk map prediction of granularity g .

Next, to model the problem comprehensively, we design a multivariate hierarchical loss function, which consists of three parts: weighted mean squared error $loss_{wmse}$, binary cross entropy $loss_{bce}$, and hierarchical constraint $loss_{hc}$:

Weighted Mean Squared Error: Motivated by [31], to give higher emphasis to high-risk accident areas and address the issue of zero inflation, we classify all accident samples into four levels based on their risks and assign different weights to them:

$$loss_{wmse} = \frac{1}{N_g} \sum_{i \in I} \lambda_i (A_g(i) - \hat{A}_g(i))^2 \quad (15)$$

where \hat{A}_g and A_g are the prediction and ground truth of granularity g , $A_g(i)$ and λ_i are the samples and weight whose traffic accident risk level is i , and N_g is the number of regions of granularity g .

Binary Cross Entropy: Different from the global perspective in $loss_{wmse}$, we utilize binary cross entropy to measure the accuracy of predicting the occurrence of traffic accidents:

$$loss_{bce} = -\frac{1}{N_g} \sum_{i=1}^N (A_g^i \log \hat{A}_g^i + (1 - A_g^i) \log(1 - \hat{A}_g^i)) \quad (16)$$

where \hat{A}_g^i and A_g^i are the prediction and ground truth of region U_i .

Hierarchical Constraint: To fully utilizing our multi-granularity hierarchical structure, we construct hierarchical constraint by utilizing the consistency between adjacent granularity level prediction results. Specifically, only the constraint between the finest-grained level g^1 and second-fine-grained level g^2 are considered since their number of regions is sufficient, which can be formulated as follows:

$$loss_{hc} = \frac{1}{N_{g^2}} (A_{g^2} - \hat{A}_{g^1} M_{tran}) \quad (17)$$

where A_{g^2} is ground truth of granularity g^2 , \hat{A}_{g^1} is the prediction of granularity g^1 , M_{tran} is the granularity transformation matrix computed by equation 8.

By combining the three mentioned loss functions, the final loss function is defined as follows:

$$loss_F = \sum_{i=1}^n (\lambda_w^i loss_{wmse}^i + \lambda_b^i loss_{bce}^i) + \lambda_{hc} loss_{hc} \quad (18)$$

where λ_w^i and λ_b^i are the weights of loss at granularity g^i , λ_{hc} and $loss_{hc}$ are the weight and hierarchical constraint.

Table 1: Statistics of Datasets

Dataset	NYC	Chicago
Time Span	1/1/2013-12/31/2013	2/1/2016-9/30/2016
Accidents	147K	44K
Taxi Orders	173,179K	1744K
POIs	15625	None
Hours of Weather	8760	5832
Road Segments	103K	56K
RS Images	400	400

4 EXPERIMENTS

4.1 Datasets

As shown in Table 1, we use two large public real-world datasets collected from NYC¹ and Chicago². The traffic accident data contains date, time, latitude and longitude, and the number of casualties. The taxi order data includes location and time of pick-up and drop-offs, which is used to calculate the traffic flow. The POI data has seven categories: residence, school, culture facility, recreation, social service, transportation and commercial. The weather data contains temperature and sky condition (i.e., sunny, rainy, cloudy, snowy and foggy). Note that for Chicago, POI data is lacking, so we only construct the road-view and risk-view semantic similarity graph. The road segment data includes road types, length and width, and snow removal priority. For remote sensing image data, we get the images of corresponding time from Google Earth.

4.2 Evaluation Metrics

To evaluate the performance of our model, we utilise three commonly used metrics for traffic accident risk prediction task [5, 23, 26, 31, 32], namely RMSE, Recall and MAP. From the perspective of regression, RMSE is used to evaluate the overall prediction of traffic accident risk. From the perspective of ranking and classification, we use Recall to evaluate classification accuracy for accident area prediction, and use MAP to evaluate ranking accuracy for high accident risk areas prediction. Lower RMSE indicates that the model can predict risk more accurately overall, while a higher Recall and MAP indicate the better performance in high-risk regions, which can be considered having better coping abilities for zero-inflation problem. The three metrics are computed as follows: $RMSE = \sqrt{\frac{1}{T} \sum_{t=1}^T (A_t - \hat{A}_t)^2}$, $Recall = \frac{1}{T} \sum_{t=1}^T \frac{S_t \cap R_t}{|R_t|}$, $MAP = \frac{1}{T} \sum_{t=1}^T \frac{\sum_{j=1}^{|R_t|} pre(j) \times rel(j)}{|R_t|}$, where A_t is the ground truth and \hat{A}_t is the predicted values at time interval t . R_t is the set of regions where traffic accidents have actually occurred at time interval t . S_t is a set of regions with top $|R_t|$ highest predicted risks. $pre(j)$ denotes the precision of a cut-off rank list from 1 to j . $rel(j) = 1$ if there are traffic accidents in region j , otherwise $rel(j) = 0$.

Furthermore, we record the above metrics specifically on the rush hours during which the frequency of traffic accidents are usually higher, i.e., 7:00-9:00 and 16:00-19:00, and for simplicity we name them as RMSE*, Recall*, and MAP*, respectively.

4.3 Experimental Settings

We partition all data into training, validation and test set with the ratio of 6:2:2. The city region is divided into grids with a size of

¹<https://opendata.cityofnewyork.us/>

²<https://data.cityofchicago.org/>

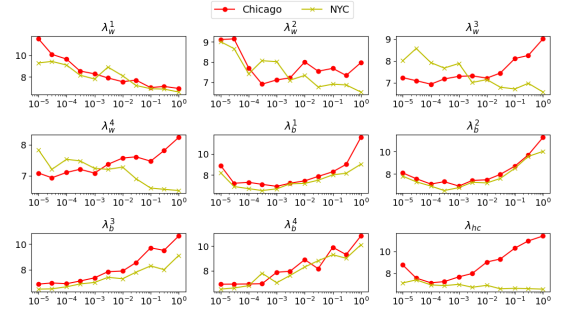


Figure 7: RMSE for Chicago and NYC vs. the Loss Weight

1982.5m × 2776.5m for NYC and 2315m × 2828m for Chicago. The time interval is one hour. The length of short-term p and long-term q are set to 3 and 4. The number of granularity levels is set to 4. In the weighted mean squared error, the weights λ_i are respectively set to 0.05, 0.2, 0.25 and 0.5. For the multi-level embedding fusion mechanism, λ_f and λ_c are set to 0.8 and 0.2, respectively.

All deep learning methods were implemented with PyTorch 1.12 and Python 3.8, and trained with a Tesla V100 GPU. The platform ran on Ubuntu 18.04. In addition, we used Adam [16] as the optimization method with the mini-batch size of 32. The learning rate is set as 0.0001, and the training epoch is set as 70. The code and data is available at <https://github.com/faceless0124/MGHSTN>.

4.4 Baseline Methods

We compare our model with the following baselines.

- **Avg**: The traffic accident risk is predicted by averaging short-term and long-term historical observations.
- **GRU** [7]: Gated Recurrent Unit. It can model historical sequential data to capture temporal dependencies.
- **H-ConvLSTM** [38]: It combines CNN with LSTM and uses a sliding window to capture the heterogeneity of different regions.
- **SDCAE** [4]: It captures the spatial features between different regions by stacking multiple denoise convolution layers.
- **GSNet** [31]: A model that captures spatio-temporal correlations from both geographic and semantic aspects.
- **MVMT-STN** [32]: A recent multi-task learning framework which can predict fine- and coarse-grained citywide traffic accident risks simultaneously to alleviate the sparsity issue.
- **C-ViT** [26]: A recent model that re-formulates the traffic accident risk prediction problem as image regression problem, and uses a contextual vision transformer to model the task.
- **HintNet** [1]: A recent hierarchical knowledge transfer network uses spatial partitioning to separate sub-regions and leverages spatio-temporal and graph convolutions.
- **RiskContra** [5]: The state-of-the-art method that employs a contrastive learning framework with multi-kernel networks to enhance risk sample representation.

4.5 Effectiveness of Loss Weight

To fine-tune the loss weight λ_w^i , λ_b^i and λ_{nc} , we vary it from 0 to 1. We compute RMSE on the validation set, and the result is plotted in Fig. 7. One can see that the loss weights have different impact on two datasets, and these three types of losses are effective

Table 2: Performance comparison of different models.

Model	NYC						Chicago					
	RMSE	Recall	MAP	RMSE*	Recall*	MAP*	RMSE	Recall	MAP	RMSE*	Recall*	MAP*
Avg	10.3243	29.42%	0.1336	9.4994	30.90%	0.1346	12.9581	16.58%	0.0622	10.2564	19.89%	0.0844
GRU	8.6782	28.76%	0.1234	7.1463	30.97%	0.1321	11.5774	17.41%	0.0652	8.7592	19.63%	0.0701
H-ConvLSTM	7.9126	30.22%	0.1454	7.2219	31.55%	0.1509	11.3002	17.82%	0.0698	8.8920	18.97%	0.0770
SDCAE	7.9965	30.87%	0.1567	7.1654	31.05%	0.1546	11.4678	18.23%	0.0709	8.6412	20.17%	0.0924
GSNet	7.6153	33.16%	0.1787	6.7760	34.15%	0.1769	10.9659	19.92%	0.0671	8.3305	21.12%	0.0745
MVMT-STN	10.3335	33.75%	0.1884	9.5021	35.09%	0.1864	13.0719	20.75%	0.0828	10.2665	22.22%	0.0931
C-ViT	8.5015	30.59%	0.1632	7.0144	31.66%	0.1577	11.7730	19.94%	0.0787	8.2250	19.91%	0.0855
HintNet	8.7562	32.81%	0.1732	7.0819	34.21%	0.1687	11.5860	19.13%	0.0817	8.6250	22.01%	0.0895
RiskContra	7.4014	34.21%	0.1854	6.7207	35.31%	0.1914	10.3564	21.20%	0.0919	7.6165	22.17%	0.0817
MGHSTN	6.8860	34.59%	0.1985	6.4511	35.67%	0.1934	7.4771	21.32%	0.0886	5.9452	22.36%	0.0946
Avg+RS	10.3243	29.42%	0.1336	9.4994	30.90%	0.1346	12.9581	16.58%	0.0622	10.2564	19.89%	0.0844
GRU+RS	8.5912	29.81%	0.1284	7.2413	31.46%	0.1387	11.2961	18.21%	0.0702	8.3781	19.37%	0.0794
H-ConvLSTM+RS	7.8906	30.39%	0.1424	7.0288	32.35%	0.1561	11.2702	18.07%	0.0723	8.6761	19.26%	0.0869
SDCAE+RS	7.7135	31.13%	0.1603	7.0890	31.75%	0.1599	11.1701	18.70%	0.0769	8.6080	20.37%	0.1031
GSNet+RS	7.5048	33.60%	0.1837	6.7290	35.37%	0.1835	10.8481	21.05%	0.0826	8.1437	22.63%	0.1065
MVMT-STN+RS	10.2213	33.98%	0.1904	9.3032	35.24%	0.1813	13.0056	<u>21.62%</u>	0.0940	10.2112	<u>23.44%</u>	<u>0.1201</u>
C-ViT+RS	8.1772	29.60%	0.1612	7.2183	31.95%	0.1522	11.5853	20.37%	0.0862	8.5841	20.42%	0.0856
HintNet+RS	8.0123	32.69%	0.1802	6.6801	34.57%	0.1729	11.0810	20.83%	0.0839	8.3109	22.71%	0.0958
RiskContra+RS	7.2017	34.51%	0.1897	6.5314	35.52%	0.1921	10.0721	21.37%	<u>0.0992</u>	7.4985	22.87%	0.1024
MGHSTN+RS	6.5011	34.74%	0.1961	5.9947	35.86%	0.1950	6.9211	21.71%	0.1054	5.1098	23.46%	0.1329

for performance improvement, especially the WMSE of the finest-grained level and BCE. Based on the results, (1) for Chicago, we set $\lambda_w^1 = 1, \lambda_w^2 = 3e - 4, \lambda_w^3 = 1e - 4, \lambda_w^4 = 3e - 5, \lambda_b^1 = 1e - 3, \lambda_b^2 = 1e - 3, \lambda_b^3 = 1e - 5, \lambda_b^4 = 1e - 5, \lambda_{hc} = 3e - 4$, (2) for NYC, we set $\lambda_w^1 = 1, \lambda_w^2 = 1, \lambda_w^3 = 1, \lambda_w^4 = 1, \lambda_b^1 = 3e - 4, \lambda_b^2 = 3e - 4, \lambda_b^3 = 1e - 5, \lambda_b^4 = 1e - 5, \lambda_{hc} = 1$.

4.6 Effectiveness Comparison

Since we innovatively introduce remote sensing data, while other methods do not, for fairness, we also introduce remote sensing data in the same way (i.e remote sensing enhancement) for the baseline methods. Table 2 shows the results of different models with and without remote sensing. we have the following observations:

- (1) **Avg** is worse than any other deep learning based methods, since it does not utilize spatio-temporal features and cannot learn the spatio-temporal correlations of traffic accidents.
- (2) **GRU** and **H-ConvLSTM** have relatively poor performance among learning-based methods. Although they outperform **Avg** on RMSE, they underperform **Avg** in some cases on Recall and MAP, indicating that they suffer from zero-inflation problem.
- (3) Whether using remote sensing, **MGHSTN** outperforms other models overall. For example, **MGHSTN+RS** outperforms the best existing methods **RiskContra+RS** by 59.6% on RMSE on Chicago, and also achieves significant improvement on Recall and MAP. Our model can make more accurate overall predictions while effectively dealing with the zero-inflation problem.
- (4) Remote sensing enhancement has improved the performance of nearly all methods, proving the effectiveness of introducing the regional background. The improvement is particularly obvious for Chicago. This may be because the addition of remote sensing images also alleviates the impact of the lack of POI data.
- (5) The performance of all methods on NYC is better than that on Chicago. The reason is two-fold: first, Chicago lacks POI data

Table 3: Efficiency of Different Methods

Model	memory size (NYC/Chicago)	training time (NYC/Chicago)	prediction time (NYC/Chicago)
Avg	1.2GB/1.1GB	None	0.01s/0.01s
GRU	8.4GB/10.3GB	28.92s/20.38s	0.05s/0.06s
H-ConvLSTM	9.5GB/10.9GB	37.72s/28.44s	0.07s/0.09s
SDCAE	9.1GB/10.2GB	34.48s/27.47s	0.06s/0.09s
GSNet	9.9GB/11.1GB	37.32s/28.34s	0.07s/0.09s
MVMT-STN	11.4GB/12.5GB	48.79s/32.76s	0.10s/0.11s
C-ViT	5.4GB/5.4GB	15.84s/10.68s	0.02s/0.02s
HintNet	10.3GB/11.7GB	38.83s/30.47s	0.07s/0.10s
RiskContra	10.8GB/11.9GB	39.31s/32.59s	0.09s/0.13s
MGHSTN	8.0GB/9.3GB	30.21s/24.85s	0.05s/0.08s

compared to NYC; second, NYC dataset contains a higher number of accidents, which allows the model to learn better.

4.7 Efficiency Comparison

For efficiency evaluation, we record the memory size, training time and prediction time. The memory size represents the required memory for training. The training time is the average time cost of an epoch. The prediction time is the time to predict all regions for one time interval. Note that the pre-training of the autoencoder introduced in 3.1.4 is conducted in advance, hence it does not incur additional time costs. The results are reported in Table 3. We observe the following:

- (1) The learning-based models for Chicago is larger than that for NYC, while the training time for Chicago is shorter. That is because compared to NYC, Chicago has fewer accidents, making it more difficult to predict but more efficient to train on. Thus, we chose a slightly larger version of all models for Chicago.
- (2) **MGHSTN** is more efficient than almost all learning based methods except **C-ViT**, since **C-ViT** trades performance for efficiency by re-formulating the problem as an image regression problem.

4.8 Ablation Study

In this section, we perform ablation experiments to verify the effectiveness of different components. We remove multi-view semantic

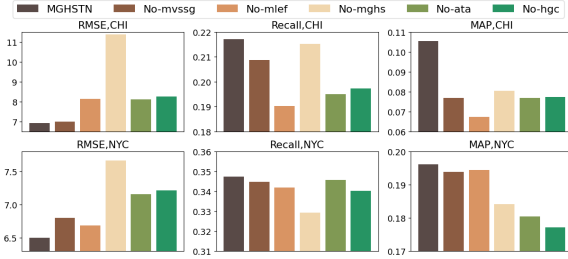


Figure 8: Ablation study of MGHSTN

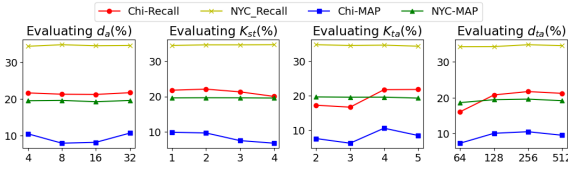


Figure 9: Recall & MAP vs. Hyper-parameter

similarity graph, multi-level embedding fusion, multi-granularity hierarchical structure, and adaptive temporal attention module respectively as four variant models, namely no-mvssg, no-mlef, no-mghs, and no-ata. In addition, to verify the effectiveness of *hierarchical graph clustering* proposed in 3.1.5, we adapt uniform clustering based on spatial proximity as an alternative, namely no-hgc. From Fig. 8, we have the following observations:

(1) **MGHSTN** outperforms the five variants on all metrics. In particular, the multi-granularity hierarchical structure is very critical, removing it will lead to 64.5% performance loss on RMSE of Chicago. Meanwhile, removing the multi-level embedding fusion significantly reduce Recall and MAP, demonstrating its ability to address the zero-inflation problem.

(2) As shown by result of no-hgc, replacing the *hierarchical graph clustering* with uniform clustering leads to a degradation in performance. This indicates that our meticulously designed hierarchical graph clustering method is capable of effectively providing a more subtle hierarchical data structure.

4.9 Hyper-parameter Study

we consider the following hyper-parameters: (1) the enhancement channels d_a of remote sensing enhancement; (2) the number of convolutions layers K_{st} in grid convolution; (3) the number of transformer encoders K_{ta} in adaptive temporal attention module; (4) the size d_{ta} of feed forward in self-attention blocks. As shown in Fig. 9, we plot the Recall and MAP for different hyper-parameters. In summary, we set each hyper-parameter to the optimal: (1) For Chicago, we have $d_a = 32$, $K_{st} = 2$, $K_{ta} = 4$, $d_{ta} = 256$. (2) For NYC, we have $d_a = 8$, $K_{st} = 2$, $K_{ta} = 2$, $d_{ta} = 256$.

5 RELATED WORK

Traffic accident risk prediction is an important topic that has been widely studied. Related work can be mainly divided into two categories: *statistics-based* and *learning-based*.

5.1 Statistics-based Methods

The *statistics-based* methods include decision tree, SVM, k-nearest neighbor and negative binomial regression. Chong et al. [6] used decision tree and ANN model to discover new knowledge from historical data about accidents. Sharma et al. [27] leverage support vector machines (SVM) with gaussian kernel to predict traffic accident risk. The authors in [22] identified the traffic accident potential by using the k-nearest neighbor method with real-time traffic data. Caliendo et al. [3] apply Poisson, negative binomial and negative multinomial regression models to tangents and curves respectively to predict traffic accidents. However, these works simply applied traditional statistical methods without considering the complex spatio-temporal correlation of traffic accidents and features, resulting in poor performance.

5.2 Learning-based Methods

In recent years, many studies have focused on using learning-based models. For spatio-temporal prediction, many researchers employ different techniques [13, 20, 25, 34–37] to model the complex spatio-temporal correlations. Early researchers employ CNN and RNN to model spatiotemporal relationships [4, 38]. To further enhance the modeling of geographical and semantic correlations, Wang et al. [31] introduce GSNet, which utilizes a weighted loss function to tackle the zero-inflation issue. Additionally, a multi-view multi-task model was proposed by [32], enabling simultaneous prediction of urban fine-grained and coarse-grained traffic accident risks. Incorporating advances in computer vision, [26] present an efficient vision transformer model, C-ViT, which processes risk map multi-channel images as input and output. Furthermore, [1, 9, 28] utilize different network to capture traffic risk patterns and dependencies. Recently, Chen et al. [5] propose RiskContra, a contrastive learning approach with multi-kernel networks, which applies contrastive learning approach to leverages the periodic patterns to derive a tailored mixup strategy for risk sample augmentation. Moreover, as for related research areas like traffic prediction, multi-task learning and urban anomaly prediction, many recent studies leverage different methods to design learning-based models [8, 11, 12, 14, 24, 39, 40].

6 CONCLUSION

We studied the traffic accident risk prediction problem for urban region. We proposed a comprehensive and novel model MGHSTN that is able to fully exploit spatio-temporal features by considering four significant aspects: regionality, proximity, similarity and sparsity. First, we introduced remote sensing images to capture regional background. Second, we designed two kinds of hierarchical structures for region feature and graph feature along with encoding methods tailored to them, and introduced multiple high-level prediction tasks to enhance the prediction. Third, we designed multivariate hierarchical loss function to model the problem comprehensively. Extensive experiments on real datasets verified effectiveness, efficiency and robustness of our model.

Acknowledgments

This work is supported by the National Natural Science Foundation of China under Grant No. 62032003 and Grant No. 61921003. Zhifeng Bao is supported in part by ARC DP220101434 and DP240101211.

References

- [1] Bang An, Amin Vahedian, Xun Zhou, W. Nick Street, and Yanhua Li. 2022. Hint-Net: Hierarchical Knowledge Transfer Networks for Traffic Accident Forecasting on Heterogeneous Spatio-Temporal Data. In *SIAM*. 334–342.
- [2] Lei Jimmy Ba, Jamie Ryan Kiros, and Geoffrey E. Hinton. 2016. Layer Normalization. In *CoRR*, Vol. abs/1607.06450.
- [3] Ciro Caliendo, Maurizio Guida, and Alessandra Parisi. 2007. A crash-prediction model for multilane roads. In *Accident Analysis & Prevention*, Vol. 39. 657–670.
- [4] Chao Chen, Xiaoliang Fan, Chuanpan Zheng, Lujing Xiao, Ming Cheng, and Cheng Wang. 2018. Sdcae: Stack denoising convolutional autoencoder model for accident risk prediction via traffic big data. In *CBD*. 328–333.
- [5] Changlu Chen, Yanbin Liu, Ling Chen, and Chengqi Zhang. 2023. RiskContra: A Contrastive Approach to Forecast Traffic Risks with Multi-Kernel Networks. In *PAKDD*, Hisashi Kashima, Tsuyoshi Idé, and Wen-Chih Peng (Eds.), Vol. 13938. 263–275.
- [6] Miao M. Chong, Ajith Abraham, and Marcin Paprzycki. 2004. Traffic Accident Analysis Using Decision Trees and Neural Networks. In *CoRR*, Vol. cs.AI/0405050.
- [7] Junyoung Chung, Çağlar Gülçehre, KyungHyun Cho, and Yoshua Bengio. 2014. Empirical Evaluation of Gated Recurrent Neural Networks on Sequence Modeling. In *CoRR*, Vol. abs/1412.3555.
- [8] Jinliang Deng, Xiuxi Chen, Renhe Jiang, Xuan Song, and Ivor W. Tsang. 2023. A Multi-View Multi-Task Learning Framework for Multi-Variate Time Series Forecasting. In *TKDE*, Vol. 35. 7665–7680.
- [9] Xiaowei Gao, Xinke Jiang, Dingyi Zhuang, Huanfa Chen, Shenhao Wang, and James Haworth. 2023. Spatiotemporal Graph Neural Networks with Uncertainty Quantification for Traffic Incident Risk Prediction. In *CoRR*, Vol. abs/2309.05072.
- [10] Kaiming He, Xiangyu Zhang, Shaoqing Ren, and Jian Sun. 2016. Identity Mappings in Deep Residual Networks. In *ECCV*, Vol. 9908. 630–645.
- [11] Chao Huang, Chuxu Zhang, Jiashu Zhao, Xian Wu, Nitesh V. Chawla, and Dawei Yin. 2019. MiST: A Multiview and Multimodal Spatial-Temporal Learning Framework for Citywide Abnormal Event Forecasting. In *WWW*, Ling Liu, Ryan W. White, Amin Mantrach, Fabrizio Silvestri, Julian J. McAuley, Ricardo Baeza-Yates, and Leila Zia (Eds.). ACM, 717–728.
- [12] Chao Huang, Junbo Zhang, Yu Zheng, and Nitesh V. Chawla. 2018. DeepCrime: Attentive Hierarchical Recurrent Networks for Crime Prediction. In *CIKM*, Alfredo Cuzzocrea, James Allan, Norman W. Paton, Divesh Srivastava, Rakesh Agrawal, Andrei Z. Broder, Mohammed J. Zaki, K. Selçuk Candan, Alexandros Labrinidis, Assaf Schuster, and Haixun Wang (Eds.). ACM, 1423–1432.
- [13] Nan Jiang, Haitao Yuan, Jianing Si, Minxiao Chen, and Shangguang Wang. 2024. Towards Effective Next POI Prediction: Spatial and Semantic Augmentation with Remote Sensing Data. In *CoRR*, Vol. abs/2404.04271.
- [14] Renhe Jiang, Zhaonan Wang, Jiawei Yong, Puneet Jeph, Quanjun Chen, Yasumasa Kobayashi, Xuan Song, Shintaro Fukushima, and Toyotaro Suzumura. 2023. Spatio-Temporal Meta-Graph Learning for Traffic Forecasting. In *AAAI*, Brian Williams, Yiling Chen, and Jennifer Neville (Eds.). 8078–8086.
- [15] George Karypis and Vipin Kumar. 1998. A Fast and High Quality Multilevel Scheme for Partitioning Irregular Graphs. In *SIAM*, Vol. 20. 359–392.
- [16] Diederik P. Kingma and Jimmy Ba. 2015. Adam: A Method for Stochastic Optimization. In *ICLR*.
- [17] Mark A Kramer. 1991. Nonlinear principal component analysis using autoassociative neural networks. In *AICHe journal*, Vol. 37. 233–243.
- [18] Yuxuan Liang, Zhongyuan Jiang, and Yu Zheng. 2017. Inferring Traffic Cascading Patterns. In *SIGSPATIAL*. 2:1–2:10.
- [19] Jianhua Lin. 1991. Divergence measures based on the Shannon entropy. In *IEEE Trans. Inf. Theory*, Vol. 37. 145–151.
- [20] Jiaxin Liu, Liwei Deng, Hao Miao, Yan Zhao, and Kai Zheng. 2022. Task assignment with federated preference learning in spatial crowdsourcing. In *CIKM*. 1279–1288.
- [21] Yao Lu, Pengyuan Zhou, Yong Liao, and Haiyong Xie. 2023. Spatiotemporal and Semantic Zero-inflated Urban Anomaly Prediction. In *CoRR*, Vol. abs/2304.01569.
- [22] Yisheng Lv, Shuming Tang, and Hongxia Zhao. 2009. Real-time highway traffic accident prediction based on the k-nearest neighbor method. In *ICMTMA*, Vol. 3. 547–550.
- [23] Chen Ma, Yingxue Zhang, Qinglong Wang, and Xue Liu. 2018. Point-of-Interest Recommendation: Exploiting Self-Attentive Autoencoders with Neighbor-Aware Influence. In *CIKM*. 697–706.
- [24] Hao Miao, Jiaying Shen, Jiannong Cao, Jiangnan Xia, and Senzhang Wang. 2022. MBA-STNet: Bayes-enhanced Discriminative Multi-task Learning for Flow Prediction. In *TKDE*.
- [25] Hao Miao, Yan Zhao, Chenjuan Guo, Bin Yang, Zheng Kai, Feiteng Huang, Jiandong Xie, and Christian S Jensen. 2024. A unified replay-based continuous learning framework for spatio-temporal prediction on streaming data. In *ICDE*.
- [26] Khaled Saleh, Artur Grigorev, and Adriana Simona Mihaita. 2022. Traffic Accident Risk Forecasting using Contextual Vision Transformers. In *ITSC*. 2086–2092.
- [27] Bharti Sharma, Vinod Kumar Katiyar, and Kranti Kumar. 2015. Traffic Accident Prediction Model Using Support Vector Machines with Gaussian Kernel. In *SocProS (Advances in Intelligent Systems and Computing, Vol. 437)*. 1–10.
- [28] Patara Trirat, Susik Yoon, and Jae-Gil Lee. 2023. MG-TAR: Multi-View Graph Convolutional Networks for Traffic Accident Risk Prediction. In *TITS*, Vol. 24. 3779–3794.
- [29] UNGA. 2020. Improving global road safety. (Sep 2020).
- [30] Ashish Vaswani, Noam Shazeer, Niki Parmar, Jakob Uszkoreit, Llion Jones, Aidan N. Gomez, Lukasz Kaiser, and Illia Polosukhin. 2017. Attention is All you Need. In *NIPS*. 5998–6008.
- [31] Beibei Wang, Youfang Lin, Shengnan Guo, and Huaiyu Wan. 2021. GSNet: Learning Spatial-Temporal Correlations from Geographical and Semantic Aspects for Traffic Accident Risk Forecasting. In *AAAI*. 4402–4409.
- [32] Senzhang Wang, Jiaqiang Zhang, Jiye Li, Hao Miao, and Jiannong Cao. 2021. Traffic Accident Risk Prediction via Multi-View Multi-Task Spatio-Temporal Networks. In *TKDE*.
- [33] WHO. 2018. Global status report on road safety 2018. (June 2018).
- [34] Ronghui Xu, Hao Miao, Senzhang Wang, Philip S Yu, and Jianxin Wang. 2024. PeFAD: A Parameter-Efficient Federated Framework for Time Series Anomaly Detection. In *SIGKDD*.
- [35] Du Yin, Renhe Jiang, Jiewen Deng, Yongkang Li, Yi Xie, Zhongyi Wang, Yifan Zhou, Xuan Song, and Jedi S. Shang. 2023. MTMGNN: Multi-time multi-graph neural network for metro passenger flow prediction. In *Geoinformatica*, Vol. 27. 77–105.
- [36] Haitao Yuan and Guoliang Li. 2021. A Survey of Traffic Prediction: from Spatio-Temporal Data to Intelligent Transportation. In *Data Sci. Eng.*, Vol. 6. 63–85.
- [37] Haitao Yuan, Guoliang Li, Zhifeng Bao, and Ling Feng. 2021. An Effective Joint Prediction Model for Travel Demands and Traffic Flows. In *ICDE*. IEEE, 348–359.
- [38] Zhuoning Yuan, Xun Zhou, and Tianbao Yang. 2018. Hetero-ConvLSTM: A Deep Learning Approach to Traffic Accident Prediction on Heterogeneous Spatio-Temporal Data. In *SIGKDD*. 984–992.
- [39] Mingyang Zhang, Tong Li, Yue Yu, Yong Li, Pan Hui, and Yu Zheng. 2022. Urban Anomaly Analytics: Description, Detection, and Prediction. In *TBD*, Vol. 8. 809–826.
- [40] Zhengyang Zhao, Haitao Yuan, Nan Jiang, Minxiao Chen, Ning Liu, and Zengxiang Li. 2024. STMGF: An Effective Spatial-Temporal Multi-Granularity Framework for Traffic Forecasting. In *CoRR*, Vol. abs/2404.05774.
- [41] Zhengyang Zhou, Yang Wang, Xike Xie, Lianliang Chen, and Hengchang Liu. 2020. RiskOracle: A Minute-Level Citywide Traffic Accident Forecasting Framework. In *AAAI*. 1258–1265.